

# Dynamics of binary black holes in young star clusters: the impact of cluster mass and long-term evolution

Stefano Torniamenti<sup>1,2,3\*</sup>, Sara Rastello<sup>1,2</sup>, Michela Mapelli<sup>1,2,3†</sup>, Ugo N. Di Carlo<sup>4,3</sup>,

Alessandro Ballone<sup>1,2,3</sup>, Mario Pasquato<sup>1,2,5</sup>

<sup>1</sup>*Physics and Astronomy Department Galileo Galilei, University of Padova, Vicolo dell'Osservatorio 3, I-35122, Padova, Italy*

<sup>2</sup>*INFN - Padova, Via Marzolo 8, I-35131 Padova, Italy*

<sup>3</sup>*INAF - Osservatorio Astronomico di Padova, Vicolo dell'Osservatorio 5, I-35122 Padova, Italy*

<sup>4</sup>*McWilliams Center for Cosmology and Department of Physics, Carnegie Mellon University, Pittsburgh, PA, 15213, USA*

<sup>5</sup>*Physics department, Montreal University, Montreal, Quebec H3T 1J4, Canada*

Accepted XXX. Received YYY; in original form ZZZ

## ABSTRACT

Dynamical interactions in dense star clusters are considered one of the most effective formation channels of binary black holes (BBHs). Here, we present direct  $N$ -body simulations of two different star cluster families: low-mass ( $\sim 500 - 800 M_{\odot}$ ) and relatively high-mass star clusters ( $\geq 5000 M_{\odot}$ ). We show that the formation channels of BBHs in low- and high-mass star clusters are extremely different and lead to two completely distinct populations of BBH mergers. Low-mass clusters host mainly low-mass BBHs born from binary evolution, while BBHs in high-mass clusters are relatively massive (chirp mass up to  $\sim 100 M_{\odot}$ ) and driven by dynamical exchanges. Tidal disruption dramatically quenches the formation and dynamical evolution of BBHs in low-mass clusters on a very short timescale ( $\lesssim 100$  Myr), while BBHs in high-mass clusters undergo effective dynamical hardening until the end of our simulations (1.5 Gyr). In high-mass clusters we find that 8% of BBHs have primary mass in the pair-instability mass gap, all of them born via stellar collisions, while only one BBH with primary mass in the mass gap forms in low-mass clusters. These differences are crucial for the interpretation of the formation channels of gravitational-wave sources.

**Key words:** black hole physics – binaries: general – galaxies: star clusters: general – stars: kinematics and dynamics – gravitational waves – methods: numerical

## 1 INTRODUCTION

Over the last six years, the LIGO (Aasi et al. 2015) and Virgo (Acernese et al. 2015) interferometers detected an increasing number of gravitational wave (GW) events (e.g., Abbott et al. 2016a; Abbott et al. 2016b; Abbott et al. 2019, 2021a). At the end of the third observing run, the third GW transient catalog (GWTC-3) consists of 90 GW candidates (Abbott et al. 2021b,c). Most of these events are produced by the inspiral of two black holes (BHs). Among the most peculiar events, the merger remnant of GW190521 (Abbott et al. 2020b; Abbott et al. 2020d) is the first intermediate-mass BH (IMBH) ever detected in the mass range  $100 - 1000 M_{\odot}$ , with a remnant mass of  $142_{-16}^{+28} M_{\odot}$ . Also, GW190412 (Abbott et al. 2020a) represents the first observation of a BBH with asymmetric masses. The population of mergers in GWTC-3 also includes two binary neutron star (BNS) mergers, GW170817 and GW190425 (Abbott et al. 2017a,b, 2020c), and two black hole-neutron star (BHNS) candidates, GW200105.162426 and GW200115.042309 (Abbott et al. 2021d). Furthermore,

Nitz et al. (2021) and Olsen et al. (2022) reported several additional GW candidates (see also Venumadhav et al. 2019, 2020; Nitz et al. 2020, 2021).

The abundance of detected GW sources allows us to attempt to reconstruct their formation channels. In fact, thanks to the distinctive features that different formation channels imprint on the merging progenitors, even a few hundreds detections may be sufficient to identify their main formation pathways (Fishbach et al. 2017; Zevin et al. 2017; Stevenson et al. 2017; Farr et al. 2017; Vitale et al. 2017; Gerosa & Berti 2017; Gerosa et al. 2018; Bouffanais et al. 2019, 2021a,b; Wong & Gerosa 2019; Wong et al. 2021; Zevin et al. 2021; Doctor et al. 2020; Kimball et al. 2020; Ng et al. 2021; Roulet et al. 2021; Mehta et al. 2022). The isolated formation scenario, for example, predicts the formation of BBHs with primary masses up to  $40 - 50 M_{\odot}$ , mostly equal-mass systems, with preferentially aligned spins and vanishingly small eccentricity in the LIGO–Virgo band (Mandel & de Mink 2016; Gerosa et al. 2018). According to this scenario, the formation of tight enough binary black holes (BBHs) can take place through evolutionary processes like common envelope (Tutukov & Yungelson 1973; Bethe & Brown 1998; Portegies

\* E-mail: stefano.torniamenti@studenti.unipd.it

† E-mail: michela.mapelli@unipd.it

Zwart & Yungelson 1998; Belczynski et al. 2002, 2008, 2010; Dominik et al. 2012, 2013; Mennekens & Vanbeveren 2014; Loeb 2016; Belczynski et al. 2016; de Mink & Mandel 2016; Marchant et al. 2016; Mapelli & Giacobbo 2018; Mapelli et al. 2019; Giacobbo & Mapelli 2018; Kruckow et al. 2018; Spera et al. 2019; Tang et al. 2020; Belczynski et al. 2020; García et al. 2021), chemically homogeneous evolution (de Mink & Mandel 2016; Mandel & de Mink 2016; Marchant et al. 2016; du Buisson et al. 2020), or stable mass transfer (e.g., Giacobbo et al. 2018; Neijssel et al. 2019; Bavera et al. 2021).

The dynamical formation scenario, instead, involves dynamical processes in dense stellar environments, like young star clusters (YSCs, e.g., Portegies Zwart & McMillan 2002; Banerjee et al. 2010; Mapelli et al. 2013; Ziosi et al. 2014; Goswami et al. 2014; Mapelli 2016; Banerjee 2017, 2018; Rastello et al. 2019; Perna et al. 2019; Di Carlo et al. 2019, 2020a; Kumamoto et al. 2019, 2020; Banerjee 2021b; Rastello et al. 2020, 2021; Dall’Amico et al. 2021; Chattopadhyay et al. 2022), globular clusters (e.g., Downing et al. 2010; Benacquista & Downing 2013; Rodriguez et al. 2015, 2016a; Antonini & Rasio 2016; Askar et al. 2017; Fujii et al. 2017; Askar et al. 2018; Fragione & Kocsis 2018; Rodriguez et al. 2019; Antonini et al. 2022), and nuclear star clusters (e.g., O’Leary et al. 2009; Miller & Lauburg 2009; McKernan et al. 2012; Arca-Sedda & Capuzzo-Dolcetta 2018; McKernan et al. 2018; VanLandingham et al. 2016; Stone et al. 2017; Hoang et al. 2018; Arca-Sedda & Gualandris 2018; Antonini et al. 2019; Arca Sedda & Benacquista 2019; Arca Sedda et al. 2020; Mapelli et al. 2021). With respect to the isolated channel, this scenario predicts the formation of merging BBHs with larger primary masses (e.g., McKernan et al. 2012; Mapelli 2016; Antonini & Rasio 2016; Gerosa & Berti 2017; Stone et al. 2017; McKernan et al. 2018; Di Carlo et al. 2019, 2020a; Rodriguez et al. 2019; Yang et al. 2019; Arca Sedda & Benacquista 2019; Arca Sedda et al. 2020; Mapelli et al. 2022), isotropic spin distributions (e.g., Rodriguez et al. 2016b), and, in some rare cases, non-zero eccentricity in the LIGO–Virgo band (e.g., Samsing 2018; Samsing & D’Orazio 2018; Samsing et al. 2018; Rodriguez et al. 2018; Zevin et al. 2019; Dall’Amico et al. 2021).

In this work, we will focus on the dynamical formation of BBHs in young and open stellar clusters. These systems are of key importance to interpret the formation of BBHs, because they host the formation of the most massive stars (Lada & Lada 2003; Portegies Zwart et al. 2010; Crowther et al. 2010), which are the progenitors of massive BHs. Thanks to the high initial central density of the host cluster ( $\rho \gtrsim 10^3 \text{ M}_\odot \text{ pc}^{-3}$ , Portegies Zwart et al. 2010), binary stars can efficiently interact with the surrounding stars since the very beginning of their life. This leaves a deep imprint on the properties of the population of BBHs and, in turn, merging BBHs. When YSCs are eventually disrupted by the tidal field of their host galaxy, their stellar content is released into the galactic field. Thus, a large fraction of BBHs which are now in the field may have formed in young stellar systems.

The dynamical formation and evolution of BBHs in YSCs are explored in a realistic way by means of direct  $N$ -body simulations, where up-to-date prescriptions for single and binary stellar evolution are implemented. In many cases, only the first few hundreds Myr of the life of the star cluster are considered. This is due, on the one hand, to their small relaxation timescales,  $t_{\text{rlx}} \lesssim 100 \text{ Myr}$  (Portegies Zwart et al.

2010). In particular, the rapid decrease of their central density within the first Myr suppresses the interaction rate in later phases, making them less and less important in shaping the BBH properties. On the other hand, producing large sets of  $N$ -body simulations, which are necessary to explore the population of merging BBHs with sufficient statistics, has high computational costs. Thus, evolving large sets of YSCs for thousands of Myr would turn to be prohibitively expensive. As a consequence, many simulation of YSCs only take into account the first 100 Myr of the star cluster life (Di Carlo et al. 2019, 2020a,b; Rastello et al. 2020, 2021).

The aim of this work is to evaluate the impact of the late phases (up to 1500 Myr) of the dynamical evolution of the star cluster on the population of BBH mergers. To this purpose, we have run two sets of  $N$ -body simulations of YSCs in different mass regimes and studied the evolution of the population of BBHs. To calculate the impact of the long-term evolution of the cluster, we compared the BBH merger populations at two different snapshots, 100 Myr and 1500 Myr. The paper is organized as follows: in Section 2, we describe the details of the  $N$ -body simulations and our method. In Section 3, we report the results for the BBH populations and mergers. Finally, Section 4 summarises our conclusions.

## 2 METHODS

### 2.1 Direct $N$ -body code

We performed our simulations with the  $N$ -body code NBODY6++GPU (Wang et al. 2015, 2016), coupled with the population synthesis code<sup>1</sup> MOBSE (Mapelli et al. 2017; Giacobbo et al. 2018; Giacobbo & Mapelli 2018). NBODY6++GPU is the GPU parallel version of NBODY6 (Aarseth 2003). It implements a 4th-order Hermite integrator, individual block time-steps (Makino & Aarseth 1992) and Kustaanheimo-Stiefel regularization of close encounters and few-body systems. The force contributions at short time steps (*irregular forces*) are computed by a neighbour scheme (Nitadori & Aarseth 2012), and for long time steps (*regular force/timesteps*) the force is evaluated by considering all the particles of the system. The irregular-force calculation is performed using CPUs, while the regular forces are evaluated on GPUs using the CUDA architecture. A solar neighbourhood-like static external field (Wang et al. 2016) is included in the force integration. This choice for the tidal field is quite conservative, because the static tidal field does not take into account possible perturbations by disk and bulge shocking, and encounters with molecular clouds, which can accelerate the star cluster disruption (Gieles et al. 2006). Orbital decay and circularization by GW emission are calculated following Peters (1964). Post-Newtonian terms are not included in this version of NBODY6++GPU.

MOBSE is a customized and upgraded version of BSE and includes up-to-date prescription for massive stellar winds (Giacobbo et al. 2018), core-collapse (Fryer et al. 2012) and electron-capture supernovae (Giacobbo & Mapelli 2019), natal kicks (Giacobbo & Mapelli 2020) and (pulsational) pair instability supernovae (Mapelli et al. 2020). Stellar winds are modeled by assuming that the mass loss of hot massive stars

<sup>1</sup> MOBSE is publicly available at [this link](#).

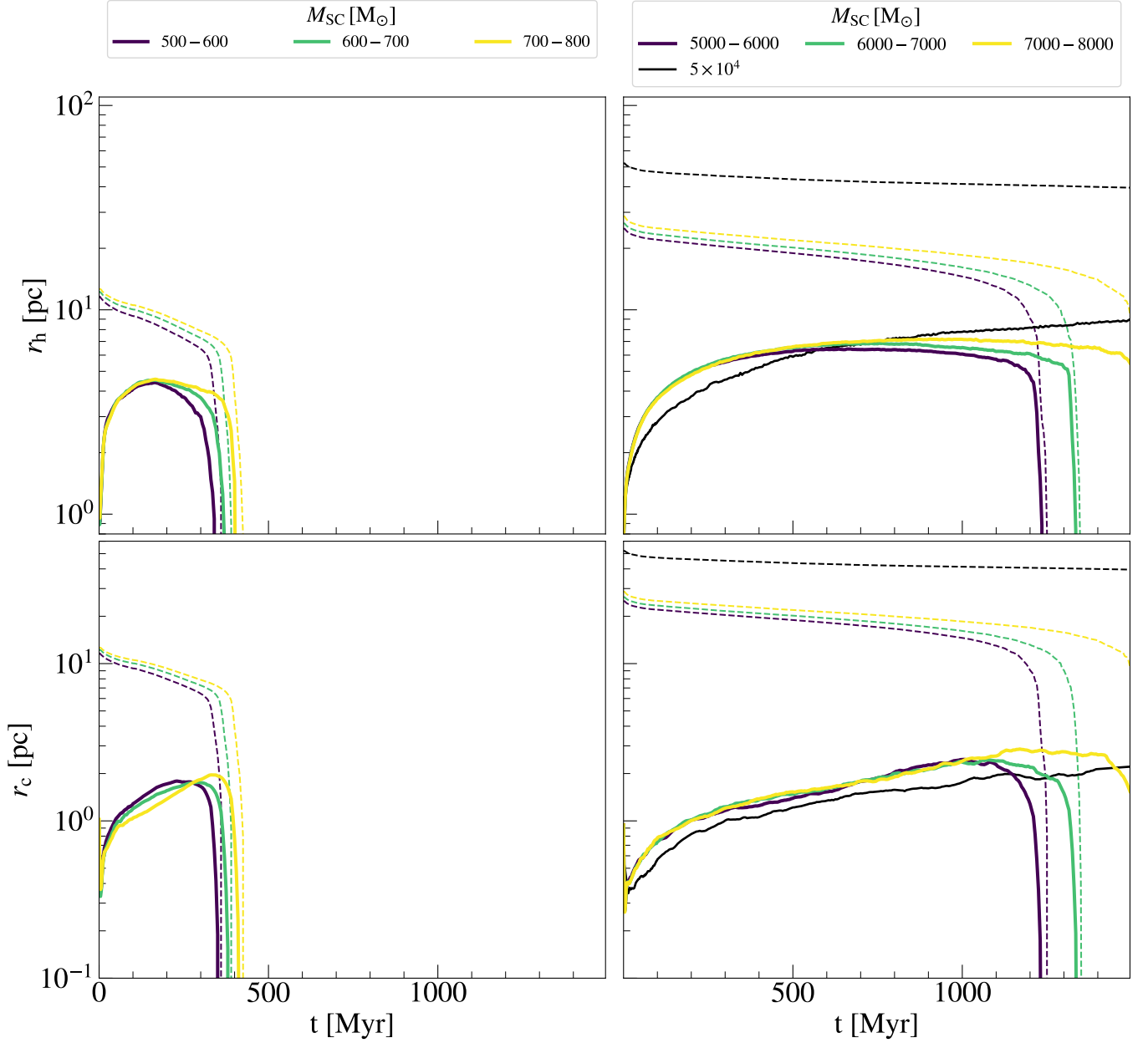


**Figure 1.** Evolution of the half-mass radius  $r_h$  (upper panels, solid lines), core radius  $r_c$  (lower panels, solid lines), and tidal radius  $r_t$  (dashed lines) for low-mass clusters (left) and high-mass clusters (right). Each set is divided into three subsets: for the low-mass clusters  $M_{\text{SC}} \in [500, 600] M_{\odot}$  (violet),  $[600, 700] M_{\odot}$  (green),  $[700, 800] M_{\odot}$  (yellow). For the high-mass clusters  $M_{\text{SC}} \in [5000, 6000] M_{\odot}$  (violet),  $[6000, 7000] M_{\odot}$  (green),  $[7000, 8000] M_{\odot}$  (yellow). Each line shows the median value over the simulated YSCs per each mass bin. The black lines (right panels) refer to the same physical quantities for the star clusters with  $M_{\text{SC}} = 5 \times 10^4 M_{\odot}$ .

depends on metallicity as  $\dot{M} \propto Z^{\beta}$ , where  $\beta$  is modelled as in [Giacobbo et al. \(2018\)](#).

For this work, we adopt the delayed model for core-collapse supernovae from [Fryer et al. \(2012\)](#). In this model, there is no mass gap between neutron stars and BHs: we assume that compact objects more massive than  $3 M_{\odot}$  are BHs. Natal kicks are modeled according to the prescription by [Giacobbo & Mapelli \(2020\)](#): the magnitude of the kick can be expressed as  $v_{\text{kick}} \propto f_{\text{H05}} m_{\text{ej}} m_{\text{rem}}^{-1}$ , where  $f_{\text{H05}}$  is a random number drawn from a Maxwellian distribution with a one-

dimensional root mean square velocity  $\sigma = 265 \text{ km s}^{-1}$ ,  $m_{\text{rem}}$  is the mass of the remnant, and  $m_{\text{ej}}$  is the difference between the final mass of the star before the supernova explosion and the mass of the remnant. Binary evolution processes (tides, mass transfer, common envelope and GW-orbital decay) are implemented as in [Hurley et al. \(2002\)](#). The common envelope process is implemented by adopting the energy formalism ([Webbink 1984](#)). In this case, we assume  $\alpha = 3$ , while the concentration parameter  $\lambda$  is calculated self-consistently as in [Claeys et al. \(2014\)](#).

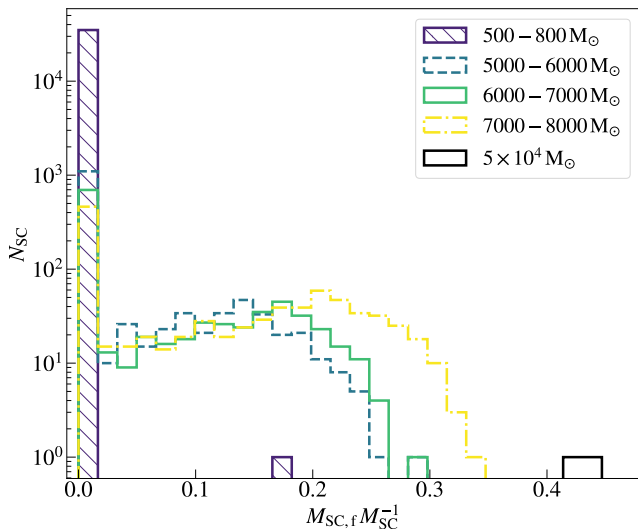


**Figure 2.** Distribution of the ratio between the star cluster bound mass at the end of the simulation,  $M_{SC,f}$ , and its initial mass  $M_{SC}$ , for stellar systems with initial mass  $M_{SC} \in [500, 800] M_{\odot}$  (violet),  $[5000, 6000] M_{\odot}$  (blue),  $[6000, 7000] M_{\odot}$  (green),  $[7000, 8000] M_{\odot}$  (yellow), and  $M_{SC} = 5 \times 10^4 M_{\odot}$  (black).

## 2.2 Initial conditions

### 2.2.1 Stellar and binary populations

We generate the initial masses of stars (single stars, primary and secondary members of binary systems) according to a Kroupa (2001) initial mass function between  $0.1 M_{\odot}$  and  $150 M_{\odot}$ . We assume a metallicity  $Z = 0.002$ , approximately corresponding to  $0.1 Z_{\odot}$ . For binary systems, we assume a distribution of mass ratios  $\mathcal{F}(q) \propto q^{-0.1}$ , with  $q \in [0.1, 1]$  (Sana et al. 2012).

Our algorithm generates a mass-dependent binary fraction  $f_b$ , according to Moe & Di Stefano (2017)<sup>2</sup>. The details of the assumed binary fraction per mass bin are shown in Table 1. We generate the orbital parameters of binary systems following the observational prescriptions by Sana et al. (2012). In particular, we randomly draw the orbital periods from:  $\mathcal{F}(\mathcal{P}) \propto \mathcal{P}^{-0.55}$ , with  $\mathcal{P} = \log_{10}(P/\text{days}) \in [0.15, 5.5]$ , and the eccentricities from  $\mathcal{F}(e) \propto e^{-0.45}$ , with  $e \in [10^{-5}, e_{\max}(P)]$ . For a given orbital period, we set an upper limit for the eccentricity distribution according to Moe & Di Stefano (2017):  $e_{\max}(P) = 1 - [P/(2 \text{ days})]^{-2/3}$ . Our method allows to obtain orbital properties for O-type stars (i.e., the progenitors of BHs) consistent with those observed in young and open clusters and OB associations (Sana & Evans 2011; Sana et al. 2012). Based on population-synthesis simulations by de Mink & Belczynski (2015), we expect that our choice of the initial binary parameters has a mild (negligible) impact on the evolution of BBHs in low-mass (high-mass) clus-

<sup>2</sup> Moe & Di Stefano (2017) take their data from different spectroscopic surveys, including binary systems in the field, OB associations, and young star clusters. Ideally, here we should consider only the sub-sample of binary systems in young star clusters (Sana et al. 2012), but this is not feasible, because the lowest-mass stars are missing in such sub-sample.

Mass Bin [ $M_{\odot}$ ]	Binary fraction $f_b$
0.1–0.8	0.2
0.8–2.0	0.4
2.0–5.0	0.59
5.0–9.0	0.76
9.0–16.0	0.84
16.0–150.0	0.94

**Table 1.** Adopted values of the original binary fraction  $f_b$  (column 2) per each stellar mass bin (column 1). From Moe & Di Stefano (2017).

ters, where binary evolution is most (least) important with respect to dynamical interactions. We refer to Torriamenti et al. (2021) for more details on our initial binary population.

### 2.2.2 Stellar clusters

We initialize stellar positions and velocities in the simulated YSCs with fractal initial conditions, with a fractal dimension  $D = 1.6$ , in order to mimic the observed clumpiness of embedded star clusters (Cartwright & Whitworth 2004; Sánchez & Alfaro 2009; Kuhn et al. 2019). We generate fractal phase space distributions with MCLUSTER (Küpper et al. 2011).

We uniformly sample the half-mass of our star clusters between 0.5 and 2 pc (e.g., Portegies Zwart et al. 2010; Krumholz et al. 2019). To evaluate the impact of long-term dynamics on the properties of BBH mergers in different dynamical regimes, we consider two sets of star clusters in different mass ranges ( $M_{SC}$ ):

- *Low-mass star clusters*, with mass ranging from  $500 M_{\odot}$  to  $800 M_{\odot}$ . These clusters present short dynamical evolution timescales at all scales: this reduces the probability of dynamical interactions and, consequently, of dynamical exchanges. Also, YSCs in this mass range typically host a few massive stars, and, consequently, BHs. This further suppresses the rate of dynamical exchanges<sup>3</sup> (Rastello et al. 2021).
- *High-mass star clusters*, with mass ranging from  $5000 M_{\odot}$  to  $8000 M_{\odot}$ . These clusters have a higher rate of dynamical encounters, as a consequence of the higher densities, longer dynamical timescales and larger number of massive stars. Thus, they are expected to produce a larger number of exchanged binaries and BBHs (Rastello et al. 2021). In this sample we also include two star clusters with mass  $5 \times 10^4 M_{\odot}$ .

Here, the terms *low-mass* and *high-mass* clusters are intended only for comparison between the two considered samples. In the literature, low-mass clusters can include even star clusters with much lower mass, down to a few ten  $M_{\odot}$  (e.g., Lada & Lada 2003), while the highest mass clusters can reach  $\sim 10^7 M_{\odot}$  (e.g., Georgiev et al. 2016).

<sup>3</sup> An exchange tends to happen when the intruder is more massive than at least one of the members of the binary system, because this leads to a substantial increase of the binary’s binding energy, hardening the binary system (Heggie 1975; Hills & Fullerton 1980; Heggie & Hut 2003). Our low-mass clusters lack massive intruders because all of the massive stars are already born in hard binary systems. Thus, exchanges tend to be suppressed.

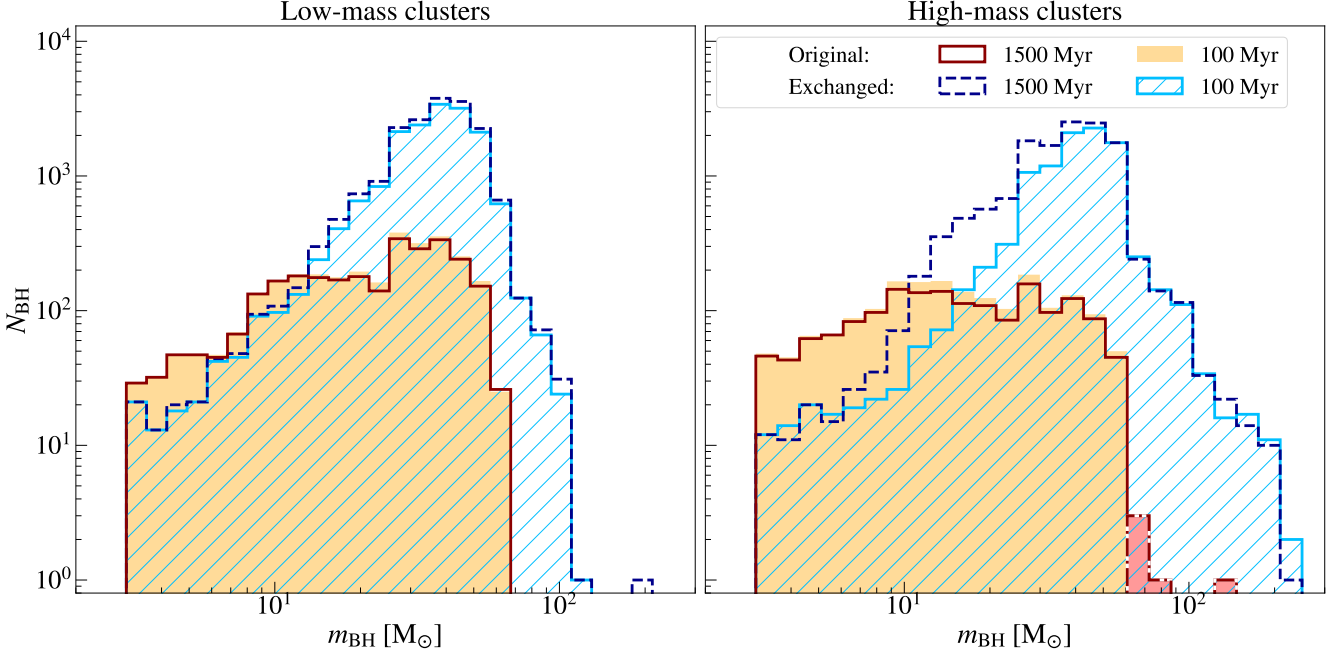


**Figure 3.** Mass distribution of BHs in BBHs, for low-mass clusters (left) and high-mass clusters (right). Red line: original BBHs at 1500 Myr. Orange filled histogram: original BBHs at 100 Myr. Blue dashed line: exchanged BBHs at 1500 Myr. Light blue hatched histogram: exchanged BBHs at 100 Myr. Among the original BHs, we highlight in red those with mass in the PI mass gap at 1500 Myr (red dash-dotted line) and at 100 Myr (red filled histogram). These are anomalous original BBHs in which one of the two stellar components has merged with another star before producing the BBH (see Section 3.2 for details).

In both cases, we sample the mass of star clusters from a power-law distribution  $dN/dM_{\text{SC}} \propto M_{\text{SC}}^{-2}$ , following Lada & Lada (2003). The two sets consist in 35578 and 3555 star clusters, respectively. The number of star clusters in the two samples is set to obtain the same total mass. The total kinetic ( $K$ ) and potential ( $W$ ) energy of the cluster are set to give a virial ratio  $Q = 2K/W = 1$ .

### 2.3 Impact of long-term evolution

The main goal of this work is to evaluate the impact of dynamics on the population of BBH mergers. In particular, we simulate our star clusters up to  $t_f = 1500$  Myr. This corresponds to a total integration time of  $\sim 150$  relaxation timescales ( $t_{\text{rlx}}$ , Spitzer 1987) for low-mass clusters which have, on average,  $t_{\text{rlx}} \sim 10$  Myr. For high-mass cluster, on average,  $t_{\text{rlx}} \sim 26$  Myr, and the total integration time is longer than  $50 t_{\text{rlx}}$ . To be completely sure that we captured all the dynamical encounters relevant for the population of BBHs, we should integrate all our clusters until they become tidally filling, or until the last BH leaves its parent cluster by ejection or evaporation. For the most massive clusters ( $> 7000 M_{\odot}$ ), our clusters become tidally filling at later times with respect to  $t_f = 1.5$  Gyr (Figure 1). However, integrating our most massive clusters for more than 1.5 Gyr currently requires prohibitive computational resources. Moreover, we found that only 0.01% (6%) of all BBHs are still bound to their parent cluster in our low-mass (high-mass) star clusters. Hence, the vast majority of our BBHs has already been

dynamically ejected at 1.5 Gyr and will not be affected by dynamical interactions at later stages.

We compare the population of BBH mergers that form in the first 100 Myr of the evolution of the simulated YSCs with the population of BBH mergers at 1500 Myr. In particular, we first evaluate the population of BBH mergers that we would have obtained if we had integrated the evolution of our YSCs only for the first 100 Myr. This population consists in:

- BBHs that merge within the first 100 Myr, during the  $N$ -body simulations.
- BBHs that will merge within a Hubble time **in absence of further dynamical interactions**. To calculate them, we consider the population of existing BBHs at 100 Myr and evolve their orbital eccentricity and semi-major axis by integrating the equations of Peters (1964), to calculate the energy loss due to GW emission:

$$\begin{aligned} \frac{da}{dt} &= -\frac{64}{5} \frac{G^3 m_1 m_2 (m_1 + m_2)}{c^5 a^3 (1 - e^2)^{7/2}} f_1(e), \\ \frac{de}{dt} &= -\frac{304}{15} e \frac{G^3 m_1 m_2 (m_1 + m_2)}{c^5 a^4 (1 - e^2)^{5/2}} f_2(e), \end{aligned} \quad (1)$$

where

$$\begin{aligned} f_1(e) &= \left( 1 + \frac{73}{24} e^2 + \frac{37}{96} e^4 \right) \\ f_2(e) &= \left( 1 + \frac{121}{304} e^2 \right). \end{aligned} \quad (2)$$

All the BBHs that merge within a Hubble time ( $t_{\text{H}} = 14$  Gyr)

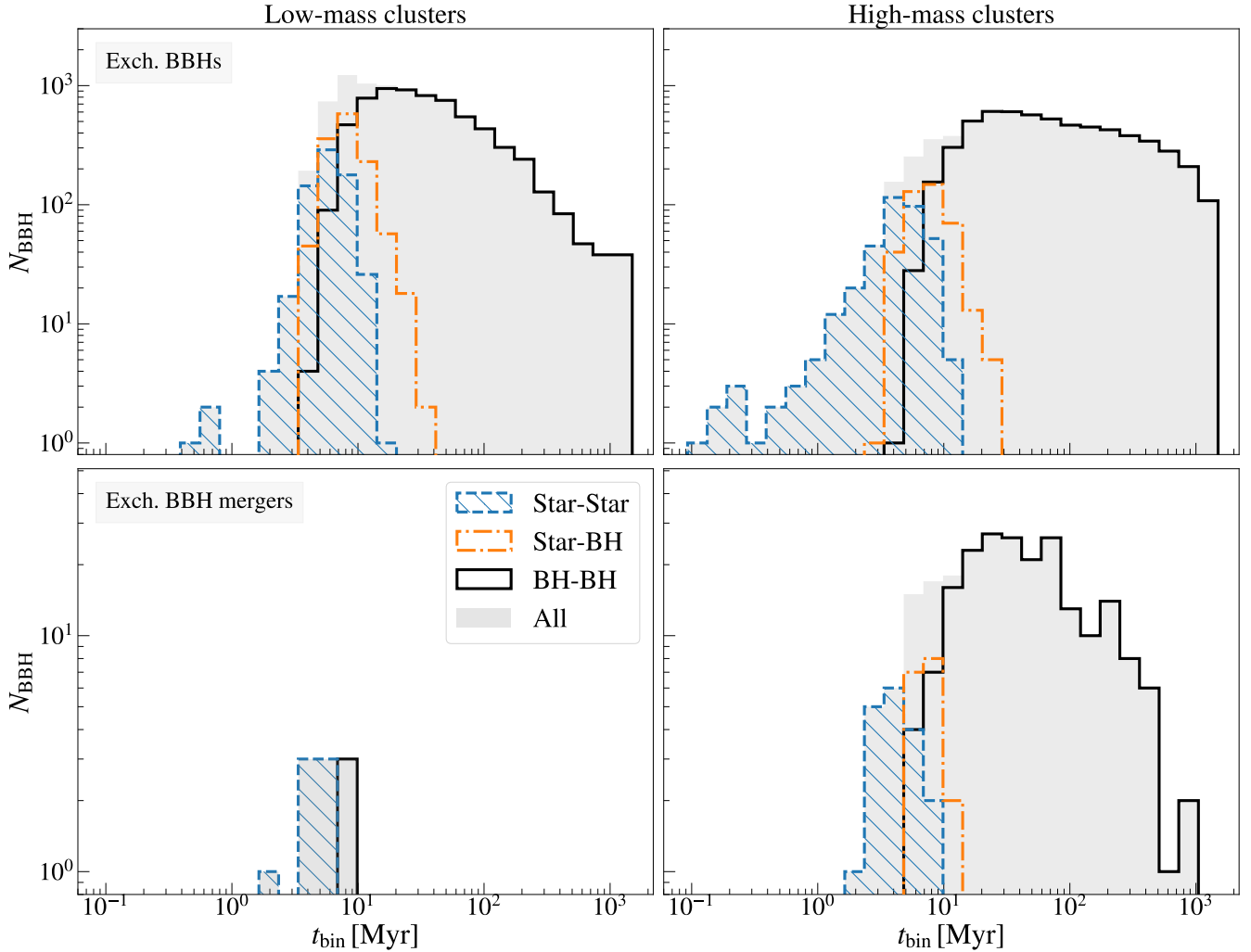


**Figure 4.** Distribution of formation times ( $t_{\text{form}}$ ) of binary systems that give birth to exchanged BBHs, in low-mass clusters (left) and high-mass clusters (right). Upper panels: all exchanged BBHs. Lower panels: exchanged BBH mergers. Blue dashed line and hatched area: BBHs that formed when both components were stars. Orange dot-dashed line: BBHs that formed when one component was a star and the other was a BH. Black line: BBHs that formed when both components were BHs. Grey area: all BBHs.

are classified as mergers. This is equivalent to assume that the YSCs dissolve at 100 Myr, and their BBHs evolve only via GW emission (no dynamical interactions) after the death of their parent star clusters.

To evaluate how dynamical encounters affect the distribution of BBH mergers in the late phases of the cluster life, we repeat the aforementioned procedure after 1500 Myr, i.e.

- we count how many BBHs merge within 1500 Myr, during the  $N$ -body simulations;
- we integrate the semi-major axis and eccentricity evolution of the other BBHs that are still bound at 1500 Myr, accounting for GW emission only (Peters 1964), and we count how many of them merge within one Hubble time.

If the dynamical interactions within the cluster are still effective after 100 Myr, they can affect the population of BBHs, and, consequently, of BBH mergers. In particular, dynamical processes can form new BBHs or harden the existing ones,

allowing them to merge within an Hubble time, or even before the end of the simulation, thus increasing the population of BBH mergers. In some other cases, dynamical interactions can disrupt existing BBHs, possibly removing them from the population of mergers that we estimated at 100 Myr.

#### 2.4 Estimate of relativistic kicks

When two BHs merge, the post-merger remnant receives a kick due to the asymmetric momentum dissipation by GWs (e.g., Favata et al. 2004). This recoil can reach up to thousands  $\text{km s}^{-1}$ , depending on the symmetric mass ratio and spin orientation (Campanelli et al. 2007). If the kick magnitude is larger than the escape velocity of the host star cluster, the post-merger remnant is ejected. For the star clusters considered in this work (Sect. 2.2), the initial escape velocities range from  $\sim 1$  to  $\sim 10 \text{ km s}^{-1}$ , and may rapidly decrease to zero as a consequence of cluster dissolution.

As our simulations do not include relativistic kicks, we evaluated the probability that a post-merger remnant is ejected a posteriori, using the equations reported by Maggiore (2018). In particular, for each BBH merger, we randomly draw a distribution of spin magnitudes for each component from a Maxwellian distribution: we consider two cases:  $\sigma_\chi = 0.1$  and  $\sigma_\chi = 0.01$  (see, e.g., Bouffanais et al. 2021b, for this assumption). Also, we assume that the spin directions are isotropically distributed over the sphere (e.g., Rodriguez et al. 2016b). We randomly draw  $10^5$  different spin magnitudes and orientations for each BH, and calculate the resulting relativistic kick distribution. Then, we evaluate the probability that the BH remnant is retained within the cluster, that is the probability to find a kick value lower than the escape velocity at the BBH merger.

For all our BBH mergers, we find a retention probability  $p < 2\%$  if  $\sigma_\chi = 0.1$  and  $p < 5\%$  if  $\sigma_\chi = 0.01$ . Thus, we can safely assume that all the post-merger remnants are ejected from their host cluster. Therefore, we will remove from our sample any second-generation BBH, i.e. any BBH that has at least one component resulting from a previous BBH merger.

### 3 RESULTS

#### 3.1 Global evolution of the cluster

Figure 1 shows the evolution of the half-mass radius  $r_h$ , tidal radius  $r_t$ , and core radius  $r_c$  of the two sets of clusters. Each set is split into three sub-sets of different mass in order to better take into account the impact of the cluster mass on its expansion. As a comparison for high-mass clusters, we also show the evolution of the stellar clusters with  $5 \times 10^4 M_\odot$ .

All the clusters show an initial rapid expansion due to the early mass loss caused by stellar and binary evolution (stellar winds and supernovae). This expansion is visible at all scales, but is more pronounced for  $r_h$ , consistently with the results of Chattopadhyay et al. (2022). Also, the early mass loss causes the initial steep decrease of the tidal radius.

After the most massive stars have evolved into compact remnants, the cluster enters a slower, relaxation-driven phase, as visible from the change of slope of  $r_t$ . In particular, the tendency towards energy equipartition makes the low-mass stars move altogether to the outer regions, approaching the tidal boundary, while the heavier stars and compact remnants sink at the centre of the cluster, if they are not already segregated (Spitzer 1987). As a result, stars are progressively removed by the galactic tidal field, leading to cluster dissolution. Eventually, the tidal stripping, further enhanced by the cluster mass loss, and the possible energy generation by massive BBHs within the cluster core lead the stellar cluster out of dynamical equilibrium (Giersz et al. 2019), causing an abrupt disruption of the cluster and a sharp decrease of its relevant radii.

The duration of the relaxation-driven phase depends on the initial cluster mass. For low mass clusters, the short relaxation timescales (Spitzer 1987), combined with the small initial mass, cause a rapid dissolution. Their typical lifetime is 400 Myr, with no particular distinction among the three subsets. The evolution of high-mass clusters, instead, is characterized by a much milder expansion, where the growth of  $r_h$  is balanced by tidal stripping. As a result,  $r_h$  remains almost constant (a similar trend can be seen in Banerjee 2017

for more massive clusters) for the first 1000 Myr. The cluster dissolution happens at different times, depending on the mass subset considered. The typical lifetime spans from 1250 Myr for clusters with mass  $< 6000 M_\odot$ , up to more than 1500 Myr for clusters more massive than  $7000 M_\odot$ . In contrast, the  $5 \times 10^4 M_\odot$  clusters undergo a far slower expansion and their tidal radius is almost unchanged at the end of the simulation, except for the initial rapid decrease due to stellar evolution mass loss.

In both low- and high-mass clusters, the core radius increases monotonically until the cluster is disrupted, thus lacking a clear core-collapse phase. As shown by Chattopadhyay et al. (2022), this is not unexpected for models with a large primordial binary population. In this case, primordial binaries can heat up the cluster since the very beginning of its evolution, preventing a deep core collapse.

Figure 2 shows the distribution of the ratio between the star cluster bound mass at 1500 Myr,  $M_{SC,f}$ , and its initial mass,  $M_{SC}$ . Low-mass clusters are completely disrupted by the tidal field of the host galaxy at the end of the simulation. In only one case, a core of about  $120 M_\odot$ , corresponding to 18% of the initial mass, can survive<sup>4</sup>.

As for high-mass clusters, one third of the stellar systems are still bound at the end of the simulation. In this set, the number of surviving clusters increases with the initial mass of the cluster. Also, more massive clusters can generally retain a higher fraction of mass. Finally, stellar clusters with  $5 \times 10^4 M_\odot$  preserve about half of their initial mass at 1500 Myr.

#### 3.2 BBH populations

Figure 3 shows the mass distribution of BHs in BBHs in the two considered snapshots: 100 Myr and 1500 Myr. In this section, we analyse both merging and non-merging BBHs. Among the BBH populations, we distinguish between *original BBHs*, whose progenitors were already present as binary stars in the initial conditions of the simulation<sup>5</sup>, and *exchanged BBHs*, which have formed as a consequence of dynamical exchanges.

In low-mass clusters, the BH populations in the two snapshots are almost identical, suggesting that, after 100 Myr, dynamical encounters play a negligible role in the evolution of BBHs. In contrast, high-mass clusters are still dynamically active at later phases, as indicated by the increase of the number of exchanged BHs between  $7 M_\odot$  and  $50 M_\odot$ .

The BH populations of low- versus high-mass clusters show several differences. First, low-mass clusters display a larger

<sup>4</sup> Most of the remaining mass of this interesting survivor consists of a BBH with a total mass of  $80 M_\odot$ , composed of two BHs of  $44 M_\odot$  and  $36 M_\odot$ , respectively. This BBH formed via dynamical exchange. The rest of the mass is distributed in 50 low-mass stars. This is a unique case in our sample. We may speculate that, because the BBH formed in a relatively loose environment ( $\sim 10 M_\odot \text{pc}^{-3}$ ), its high mass and the poor dynamical interaction rate allowed a number of stars to remain within the tidal radius, without being scattered away by the BBH itself.

<sup>5</sup> In the literature, a binary star that is already present in the initial conditions of a direct  $N$ -body simulation is often referred to as a primordial binary star. Here, we use the term *original* instead of *primordial*, to avoid any possible confusion with the concept of primordial BHs (e.g., Carr et al. 2016).

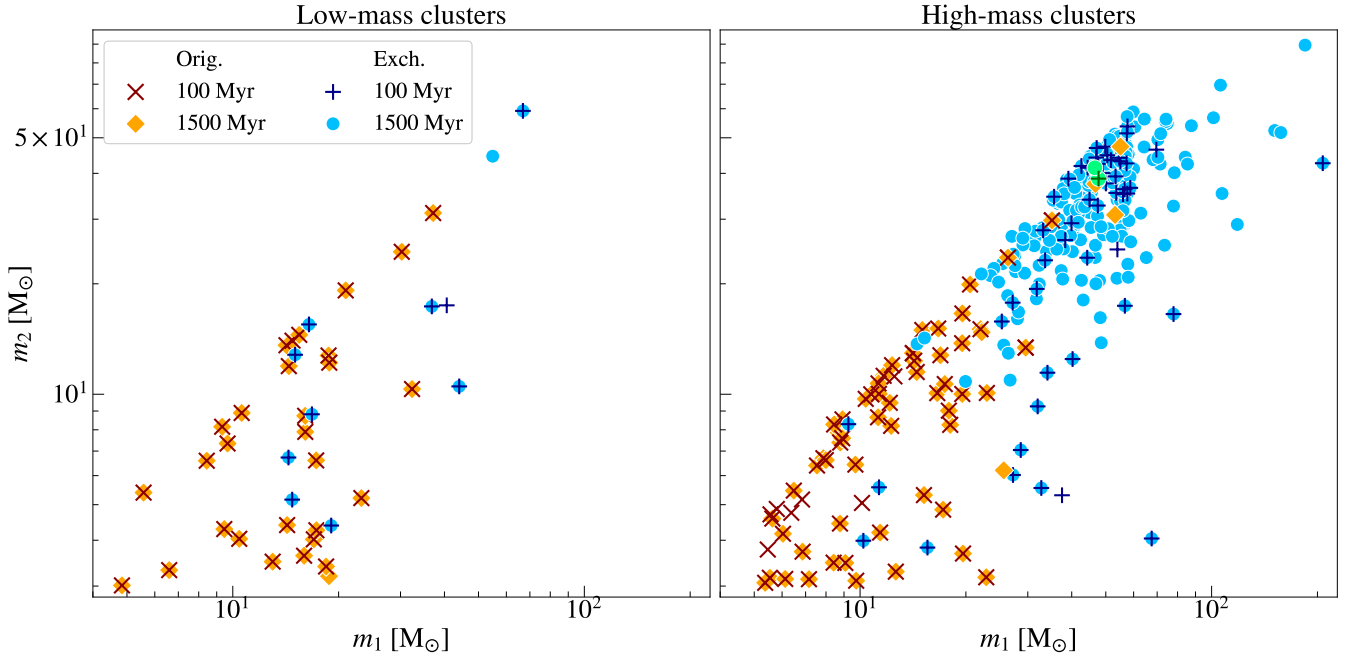


**Figure 5.** Mass of the secondary BH ( $m_2$ ) versus the primary BH ( $m_1$ ) of BBH mergers in low-mass clusters (left) and high-mass clusters (right). Orange diamonds: original BBHs at 1500 Myr. Red crosses: original BBHs at 100 Myr. Light blue circles: exchanged BBHs at 1500 Myr. Blue plusses: exchanged BBHs at 100 Myr. Green circles: exchanged BBHs at 1500 Myr in star clusters with mass  $5 \times 10^4 M_\odot$ .

number of original BBHs with  $m_{\text{BH}} > 20 M_\odot$ . Such massive original BBHs tend to be suppressed in high-mass clusters, because they undergo stronger dynamical interactions for a longer time, eventually resulting in a dynamical exchange. This leads to the formation of nearly equal-mass, massive exchanged BBHs in the high-mass clusters. This process is also enhanced by the higher initial number of massive stars in high-mass clusters with respect to low-mass clusters. As a consequence, original BBHs in high-mass clusters tend to have lower masses than those in low-mass clusters.

Figure 4 displays the distribution of formation times of the binary systems that give birth to exchanged BBHs ( $t_{\text{form}}$ ). In low-mass clusters, 8% of these systems form when both components are still stars, and about 15% when only one component is a BH. Most of the binaries that result in BBHs form by the pairing of two BHs, with a peak at formation time  $t_{\text{form}} = 10\text{--}20$  Myr. The rapid decrease of the dynamical activity and the dissolution of the stellar cluster cause a steep decrease in the distribution of  $t_{\text{form}}$ , and only 12% of the BBHs form after 100 Myr in low-mass clusters.

In high-mass clusters, about 88% of the binaries resulting in BBHs form from the pairing of two BHs. In this case, the distribution of  $t_{\text{form}}$  shows a flatter trend, hinting at an efficient dynamical activity of the cluster at later times. In fact, more than one third of the BBHs pair up after 100 Myr. In these clusters, only 5% of the binaries that produce BBH systems form when both components are still stars.

### 3.2.1 Mass-gap BHs and IMBHs

More than 7% of our simulated BBHs in high-mass clusters

(here we consider both merging and non-merging systems) have primary mass  $> 60 M_\odot$ .

The formation of such massive BHs, with mass ranging from  $\sim 60 M_\odot$  to  $\sim 120 M_\odot$  is suppressed in single stellar evolution by pair-instability (PI) and pulsational pair instability (PPI). Nonetheless, as shown by Spera et al. (2019), Di Carlo et al. (2019) and Di Carlo et al. (2020a), BHs in the mass gap can form as a consequence of stellar mergers, which produce very massive stars that eventually collapse to BHs.

BHs in this mass range may also be the result of previous BH mergers (e.g., Banerjee 2021a). However, almost all merger remnants are expected to be ejected by relativistic kicks in our simulated star clusters (Sect. 2.4). Hence, all the BHs which have a mass  $60\text{--}120 M_\odot$  and are members of BBHs form as a result of stellar mergers in our simulated star clusters.

In five cases, a BH with mass  $> 60 M_\odot$  even forms in an original binary system. These are systems in which the original binary remains bound after the merger of one of its components with a third star, producing an original binary with a mass-gap primary BH (Fig. 3).

Low-mass clusters display a lower percentage of mass-gap BHs in BBHs ( $\sim 4\%$ ), because of their lower rate of dynamical interactions as well as the limited initial number of massive stars (Sect. 3.2). Also, no mass-gap BH is present in original binary systems.

Furthermore,  $\sim 1.5\%$  of all BHs that are binary members in our high-mass clusters are IMBHs (i.e., BHs with mass  $> 100 M_\odot$ ). The maximum BH mass we find in BBHs in our high-mass clusters is  $250 M_\odot$ . As in the case of BHs in the PI mass-gap, all the IMBHs we found form via multiple stellar collisions (e.g., Di Carlo et al. 2021). In contrast, only



BBH mergers	Low-mass clusters		High-mass clusters	
	100 Myr	1500 Myr	100 Myr	1500 Myr
All	40	40	115	307
Original	30	30	64	60
Exchanged	10	10	51	247
Inside YSC	1	1	25	174
IMBHs	1	1	4	47
$m_{\text{tot,max}} [M_{\odot}]$	126	126	249	273

**Table 2.** We report the number of all (first row), original (second row) and exchanged (third row) BBH mergers. We also show the number of BBHs that merge inside the cluster during the simulation (fourth row) Finally, we report the number of IMBHs produced by BBH mergers (merger remnants, fifth row), and their maximum BH mass (last row).

eight BHs with mass  $> 100 M_{\odot}$  form in low-mass clusters, corresponding to  $\sim 0.1\%$  of all the BHs born in the low-mass clusters.

### 3.3 BBH mergers

In this Section, we focus on BBH mergers, i.e. BBHs that reach coalescence in less than 14 Gyr.

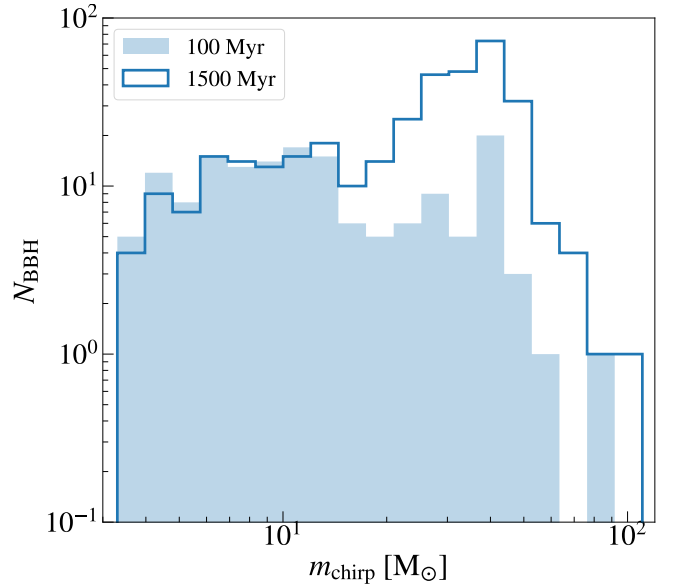
#### 3.3.1 Low-mass clusters

Figure 5 shows the mass of the secondary BH ( $m_2$ ) versus the primary BH ( $m_1$ ) for BBH mergers. In low-mass clusters, the population of BBH mergers mostly consists of original BBHs, as a further proof of the poor dynamical activity of these systems. In general, dynamical exchanges do not affect the population of BBHs after 100 Myr ( $\sim 10 t_{\text{rlx}}$ ), as already suggested by Fig. 3, with two exceptions. First, one BBH that is predicted to merge if the simulation is run only for 100 Myr, is later disrupted by dynamical interactions, and no longer exists at 1500 Myr. Also, the second most massive merger (with a final remnant mass  $m_{\text{tot}} = 99 M_{\odot}$ ) needs to dynamically harden for longer than 100 Myr to enter the regime in which the orbital decay by GWs becomes effective. As shown in Fig. 4 (lower panel), 70% of the binaries that give birth to merging BBHs form at early stages, when both components are stars. At later stages, the scarce efficiency of dynamical hardening in low-mass clusters quenches the formation of further BBH mergers.

The properties of BBH mergers are summarized in Table 2. In low-mass clusters, almost all the BBHs are no longer bound to their host cluster when they merge. In this work, a BBH merger is labelled as bound if it merges inside the cluster during the simulation.

#### 3.3.2 High-mass clusters

High-mass star clusters host a population of BBH mergers about eight times larger than low-mass clusters, although the total initial mass of the two sets of star clusters is approximately the same. This enhancement of BBH mergers in high-mass clusters is particularly evident for the exchanged systems, which, at 1500 Myr, represent the majority of BBH mergers.



**Figure 6.** Chirp mass distribution of merging BBHs at 100 Myr (light-blue filled histogram) and at 1500 Myr (blue line), for all the simulated clusters.

The populations of BBH mergers at 100 and 1500 Myr show notable differences. A number of original BBHs that, at 100 Myr, are predicted to merge are later disrupted (Figure 5 and Table 2). Some exchanged BBHs are also disrupted after the first 100 Myr. However, these disrupted exchanged BBHs are compensated by the late formation and/or hardening of other exchanged BBHs: we predict 51 exchanged BBH mergers at 100 Myr ( $\sim 4 t_{\text{rlx}}$ ), while at 1500 Myr ( $\sim 60 t_{\text{rlx}}$ ) we find five times more exchanged BBH mergers, as shown in Table 2. Figure 4 shows that most of the binaries that result in BBH mergers form via exchange when both components have already collapsed to BHs. As opposed to low-mass clusters, merging BBHs can form at very late stages, up to 1000 Myr.

A large number of BBHs (174) merge during our simulations, while they are still inside their parent cluster. Their post-merger remnant is always ejected from the cluster by gravitational recoil (see Sect. 2.4), thus preventing the possibility of second-generation BH mergers.

In high-mass clusters, 47 BBH mergers give birth to IMBHs, with a remnant mass  $m_{\text{tot}} > 100 M_{\odot}$ . In the eight most massive mergers, the primary BH is itself an IMBH. The most massive merger remnant has a mass  $m_{\text{tot}} = 273 M_{\odot}$ .

Figure 6 shows the distribution of chirp masses of BBH mergers, for the two considered snapshots (100 and 1500 Myr). The changes in the distribution are mostly due to the long-term dynamical activity within high-mass clusters. The late dynamical activity triggers a large increase of the number of mergers with high chirp mass  $m_{\text{chirp}} \approx 35 - 40 M_{\odot}$ .

### 3.4 BBH orbital properties at formation

To estimate for how long a stellar cluster is dynamically active and can affect the formation of BBH mergers, we evaluated  $t_M$ , defined as the time (since the beginning of the simulation)

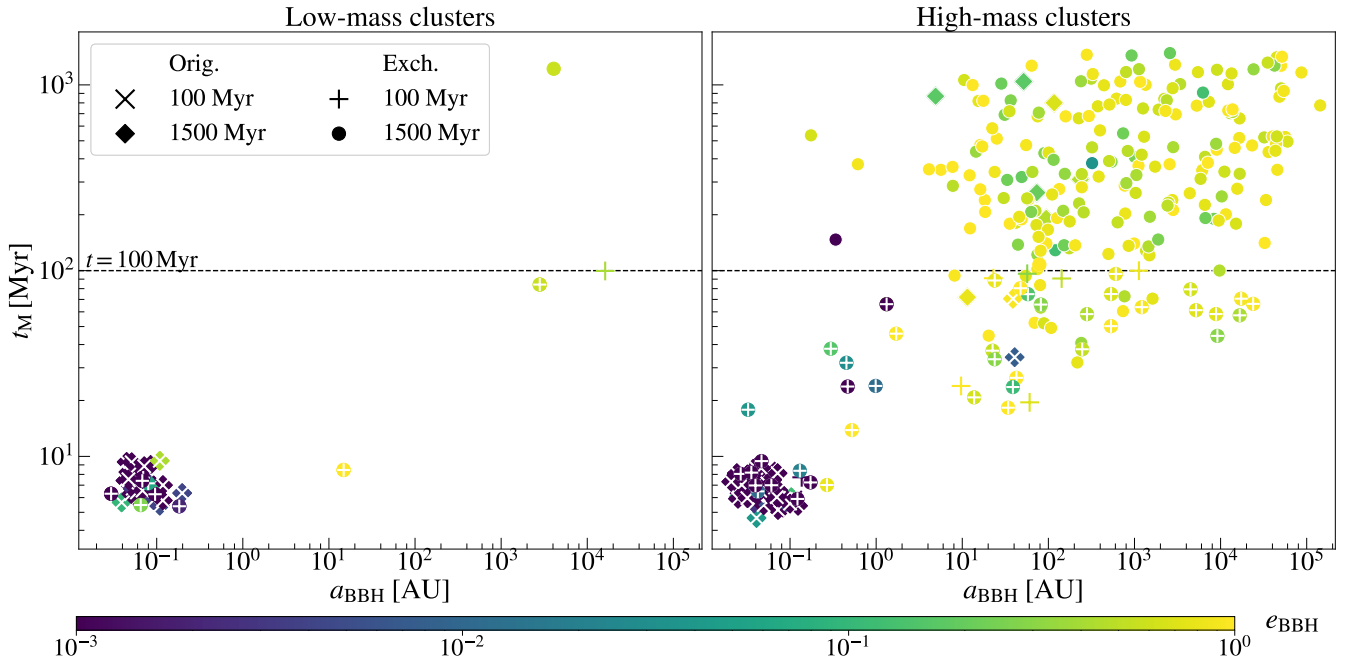


**Figure 7.** Time at which the semi-major axis of the BBH has become sufficiently tight to merge within a Hubble time via GW emission (according to Peters 1964) versus semi-major axis of the BBH when it forms ( $a_{\text{BBH}}$ ), for merging BBHs in low-mass clusters (left) and high-mass clusters (right). The markers are the same as in Figure 5. The colour-map encodes the information on the orbital eccentricity at the BBH formation,  $e_{\text{BBH}}$ . If a BBH at 1500 Myr is also present at 100 Myr, it is marked with a white cross (original) or plus (exchanged).

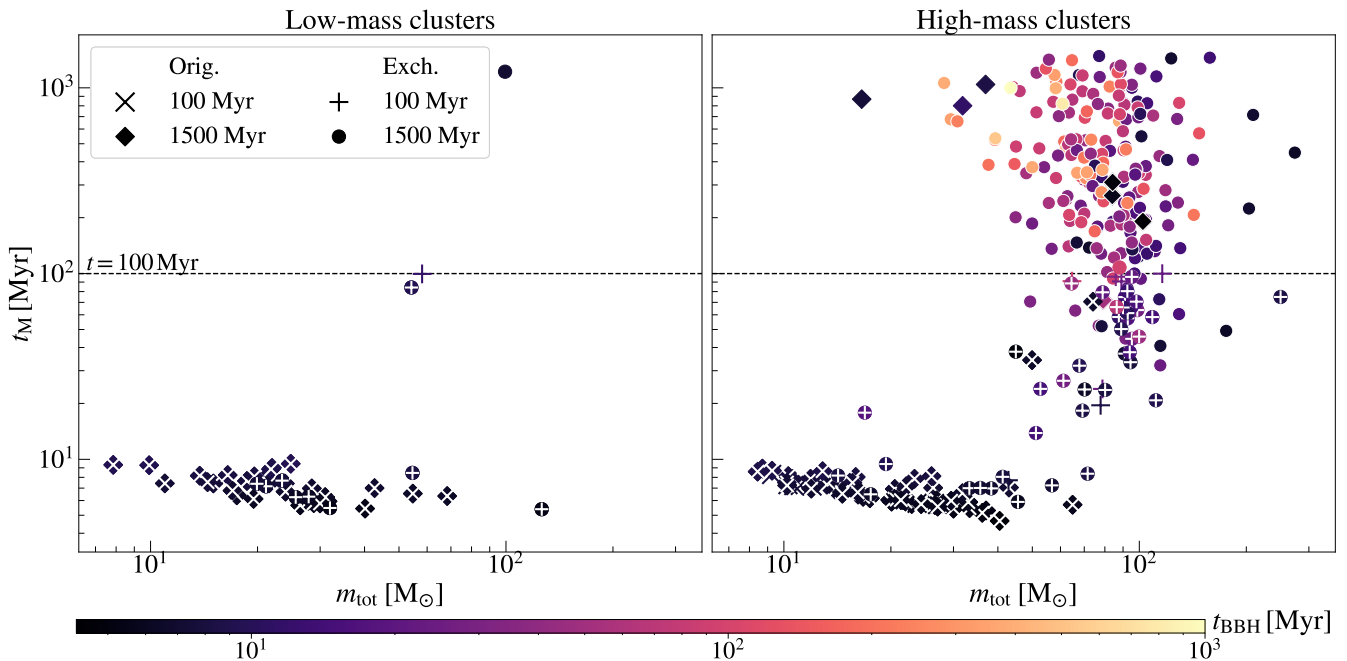


**Figure 8.** Time at which the semi-major axis of the BBH has become sufficiently tight to merge within a Hubble time via GW emission (according to Peters 1964) versus total mass of the BBH merger ( $m_{\text{tot}}$ ), for merging BBHs in low-mass clusters (left) and high-mass clusters (right). The markers are the same as in Figure 5. The colour-map encodes the information on the time at which the BBH forms,  $t_{\text{BBH}}$ . If a BBH at 1500 Myr is also present at 100 Myr, it is marked with a white cross (original) or plus (exchanged).

at which the semi-major axis of the BBH has become sufficiently tight to merge within a Hubble time via GW emission. Figure 7 shows  $t_M$  as a function of the initial orbital properties of the BBH, that is its initial semi-major axis ( $a_{\text{BBH}}$ ) and orbital eccentricity ( $e_{\text{BBH}}$ ).

In both low-mass and high-mass clusters, the original BBH mergers show typical values of  $t_M \lesssim 10$  Myr,  $a_{\text{BBH}} \lesssim 0.1$  AU, and circular orbits. These properties spring from their formation pathway. These BBHs are, in fact, the result of original binaries that hardened as a consequence of a common envelope phase. When the second BH forms, the orbital properties of the BBH already allow it to merge within an Hubble time. For this class of BBH mergers, then,  $t_M$  mainly coincides with the time at which the second BH in the binary forms. Also, because the common envelope phase leads to a large mass loss, the resulting BH masses are systematically smaller than the exchanged ones.

As a confirmation of this idea, Fig. 8 shows  $t_M$  as a function of the total mass of the merging BBH,  $m_{\text{tot}}$  and the time at which the BBH forms,  $t_{\text{BBH}}$ . Original BBHs have  $t_{\text{BBH}} \lesssim 10$  Myr and, in most cases,  $t_{\text{BBH}} = t_M$ . In high-mass stellar cluster, seven original BBHs show  $t_M > t_{\text{BBH}}$ , with  $t_M$  that can be as high as 1000 Myr. In these cases, dynamical hardening allows the binary system to enter the GW regime after the BBH formation. Because these mergers have not undergone a common envelope phase, they can have masses comparable to the exchanged BBHs (up to  $m_{\text{tot}} = 102 M_\odot$ ). In contrast,  $t_{\text{BBH}}$  ranges from 5 Myr to 1100 Myr for exchanged BBHs. In high-mass clusters, more than 20% of all BBHs form after the first 100 Myr. Because exchanged BBHs have not undergone mass loss by a common envelope phase, and because dynamical exchanges favour the formation of massive binaries, their total masses are systematically higher than those of original BBH mergers, with  $m_{\text{tot}} \gtrsim 40 M_\odot$ .

In low-mass YSCs, only three exchanged BBH mergers have  $a_{\text{BBH}} \gtrsim 1$  AU. In two cases, these mergers correspond to the two most massive BBHs, which formed in dynamically active environments. As a further proof of their dynamical origin, these BBHs are characterized by eccentric orbits. In high-mass clusters, where dynamical interactions play a major role, the distribution of BBH mergers extends to higher values of  $a_{\text{BBH}}$  and  $t_M$ . In particular, exchanged binaries, when they form, are generally characterized by large semi-major axes, up to  $1.5 \times 10^4$  AU, and thus take longer times to enter the regime in which GWs efficiently shrink the semi-major axis. In some cases,  $t_M$  can be as high as 1400 Myr, indicating that dynamical hardening can play a role even at the very end of the simulation.

Finally, the dynamical encounters that lead to the formation of BBHs leave a distinctive imprint on their eccentricity. The resulting binary systems are, in fact, characterized by larger eccentricities at formation, with  $e_{\text{BBH}} > 0.1$ <sup>6</sup>. Exchanged BBHs that have values of  $t_M \lesssim 100$  Myr and high eccentricities can be later disrupted by dynamical interactions, and are no longer present at 1500 Myr.

<sup>6</sup> In this discussion, we refer to the eccentricity at the BBH formation. During the in-spiral phase, the BBH mergers will still be circularized as a consequence of GW emission.

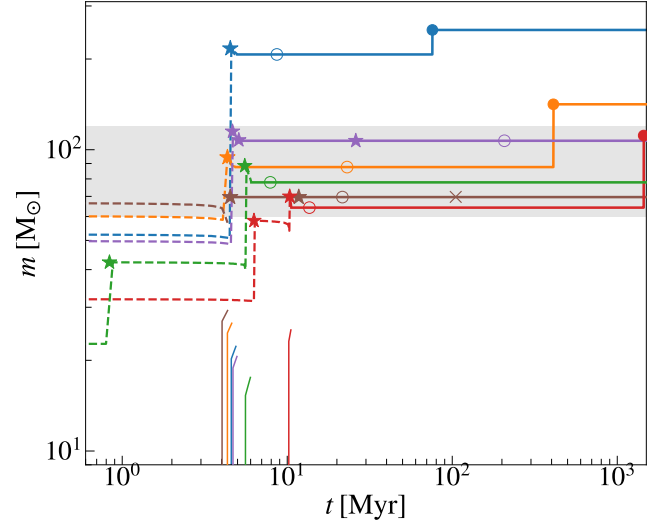


**Figure 9.** Evolution of the total mass (thick lines) and core mass (thin lines), for the progenitors of BHs in the PI mass gap and for the most massive primary component of a BBH merger (blue line). The dashed lines mark the time interval before the star becomes a BH. Different markers indicate: the merger between the progenitor star or the BH and another star (stars), the time when the BBH forms (open circles), the merger between the BH and another BH (filled circle), and the time at which the binary is possibly disrupted (crosses). The grey area encloses the PI mass gap, from  $\sim 60 M_\odot$  to  $\sim 120 M_\odot$ .

### 3.5 Formation pathway of BHs in the upper mass gap

In high-mass (low-mass) stellar clusters, the primary component of 26 BBH mergers (1 BBH merger) has mass in the PI gap. This corresponds to 8% (2.5%) of all BBH mergers in high-mass (low-mass) clusters. Figure 9 shows the evolution of some BHs in the PI mass gap that become the primary components of BBH mergers. In all cases, the progenitor star undergoes at least one collision with another star. The merger product of such stellar collisions is an exotic star, with an undersized He core with respect to the hydrogen-rich envelope. Such star does not develop PI, because its central properties (temperature and density) do not fall within the PI regime (e.g., Renzo et al. 2020; Costa et al. 2021, 2022; Ballone et al. 2022). At the end of its evolution, the stellar product directly collapses into a BH more massive than  $60 M_\odot$ .

In all our simulations, the binary system that eventually results in a BBH merger with primary mass in the PI gap forms via dynamical exchanges, when both components have already collapsed into BHs. We conservatively assume that mergers between a BH and a star do not affect the mass of the BH, because we expect mass accretion onto the BH to be very inefficient (Di Carlo et al. 2020a,b, but see Rizzuto et al. 2021 for a different assumption).

## 4 SUMMARY

We have studied the formation of BBHs in young and open star clusters via direct  $N$ -body simulations, exploiting the

codes NBODY6++GPU (Wang et al. 2015) and MOBSE (Mapelli et al. 2017). We simulated two different classes of star clusters: low-mass ( $500\text{--}800 M_{\odot}$ ) and relatively high-mass ( $5000\text{--}8000 M_{\odot}$ ) systems. We find that the properties and timescales of BBH mergers in the two star-cluster families are extremely different.

In low-mass clusters, most BBHs form in the first 100 Myr and are the result of the evolution of original binary stars, which evolve through common envelope. They do not harden significantly after  $\sim 100$  Myr. In contrast, the late evolutionary stages ( $> 1$  Gyr) are crucial for high-mass clusters. Exchanged BBHs (i.e., BBHs that form via dynamical exchanges) are the most common BBH mergers in high-mass clusters (Figures 3 and 5). While exchanged BBHs form preferentially in the first  $\sim 100$  Myr, they keep hardening significantly until the end of the simulations (1.5 Gyr, Figure 4). This confirms the importance of integrating the evolution of relatively massive clusters ( $\gtrsim 5000 M_{\odot}$ ) for  $> 1$  Gyr.

This difference between the BBH population of low-mass and high-mass star clusters mostly springs from the different two-body relaxation timescale and tidal disruption timescale of the two star cluster families. Our low-mass and high-mass star clusters have an average two-body relaxation timescale (Spitzer 1987) of  $\sim 10$  Myr and  $\sim 26$  Myr, respectively. This means that mass segregation and other dynamical processes happen earlier in low-mass clusters. Furthermore, low-mass clusters dissolve already at  $\sim 300$  Myr because of the galactic tidal field, while our high-mass clusters become tidally filling at  $\gtrsim 1200$  Myr (Figure 1). Hence, the dynamical activity of the low-mass clusters is quenched by tidal evaporation about four times earlier than that of high-mass clusters.

In both low-mass and high-mass clusters, the latest BBHs that form (exchanged BBHs) are the most massive ones (primary mass  $\gtrsim 30 M_{\odot}$ ), because dynamical exchanges favour the pairing of the most massive BHs (Figure 5). The distribution of the chirp mass of BBH mergers shows two main peaks: the main peak at  $\sim 30\text{--}40 M_{\odot}$ , and a secondary peak at  $\sim 7\text{--}15 M_{\odot}$ . The high-mass peak develops mainly after 100 Myr (Figure 6).

These results confirm that we must integrate the evolution of a star cluster for at least 50 two-body relaxation timescales if we want to probe its BBH population.

BBH mergers in low-mass clusters are driven mostly by binary evolution via common envelope: they form with short semi-major axis ( $\sim 0.1$  AU) and low orbital eccentricity (Figure 7). In contrast, massive BBHs in high-mass clusters form with larger semi-major axis ( $> 10$  AU) and higher orbital eccentricity (0.1 – 1).

A non-negligible percentage (8%) of our simulated BBH mergers in high-mass clusters have primary component's mass in the pair-instability (PI) mass gap. All of them form via stellar collisions, in which a main-sequence star merges with a more evolved star (core He burning). About 80% of these massive BBHs leave a merger remnant in the IMBH range. In contrast, in low-mass clusters only one dynamical BBH merger produces an IMBH.

Furthermore, in the high-mass clusters, we find a few original BBHs with primary mass in the PI mass gap. These are systems in which one of the two components of the binary star undergoes a collision with a third star and collapses to a BH in the PI mass gap without leading to the ionization of the original binary system.

Overall, our study shows that the formation channels of BBHs in low-mass ( $\sim 500\text{--}800 M_{\odot}$ ) and high-mass star clusters ( $\geq 5000 M_{\odot}$ ) are extremely different and lead to two completely distinct BBH populations. Low-mass clusters host mainly low-mass BBHs born from binary evolution, while BBHs in high-mass clusters are relatively massive and driven by exchanges. This difference is crucial for the interpretation of GW sources.

## ACKNOWLEDGEMENTS

We thank the anonymous referee for the insightful comments, which helped to improve the quality of this manuscript. MM, AB and SR knowledge financial support from the European Research Council for the ERC Consolidator grant DEMOBLACK, under contract no. 770017. We thank Nicola Giacobbo and the members of the DEMOBLACK team for useful discussions. We acknowledge that the results of this research have been achieved using the DECI resource Snellius based in the Netherlands at SURFSara, with support from the PRACE aisbl. MP acknowledges financial support from the European Union's Horizon 2020 research and innovation programme under the Marie Skłodowska-Curie grant agreement No. 896248. ST thanks Mark Gieles and the ICCUB Virgo team for useful comments and discussions.

## DATA AVAILABILITY

The data underlying this article will be shared on reasonable request to the corresponding authors. The latest public version of MOBSE can be downloaded from [this repository](#).

## REFERENCES

- Aarseth S. J., 2003, *Gravitational N-Body Simulations*. Cambridge University Press
- Aasi J., et al., 2015, *Classical and Quantum Gravity*, **32**, 115012
- Abbott B. P., et al., 2016a, *Physical Review X*, **6**, 041015
- Abbott B. P., et al., 2016b, *Phys. Rev. Lett.*, **116**, 061102
- Abbott B. P., et al., 2017a, *ApJ*, **848**, L12
- Abbott B. P., et al., 2017b, *ApJ*, **848**, L13
- Abbott B. P., et al., 2019, *Physical Review X*, **9**, 031040
- Abbott B. P., et al., 2020a, *Phys. Rev. D*, **102**, 043015
- Abbott R., et al., 2020b, *Phys. Rev. Lett.*, **125**, 101102
- Abbott B. P., et al., 2020c, *ApJ*, **892**, L3
- Abbott R., et al., 2020d, *ApJ*, **900**, L13
- Abbott R., et al., 2021a, arXiv e-prints, [p. arXiv:2108.01045](#)
- Abbott R., et al., 2021b, arXiv e-prints, [p. arXiv:2111.03606](#)
- Abbott R., et al., 2021c, arXiv e-prints, [p. arXiv:2111.03634](#)
- Abbott R., et al., 2021d, *ApJ*, **915**, L5
- Acernese F., et al., 2015, *Classical and Quantum Gravity*, **32**, 024001
- Antonini F., Rasio F. A., 2016, *ApJ*, **831**, 187
- Antonini F., Gieles M., Gualandris A., 2019, *MNRAS*, **486**, 5008
- Antonini F., Gieles M., Dosopoulou F., Chattopadhyay D., 2022, arXiv e-prints, [p. arXiv:2208.01081](#)
- Arca Sedda M., Benacquista M., 2019, *MNRAS*, **482**, 2991
- Arca-Sedda M., Capuzzo-Dolcetta R., 2018, *Monthly Notices of the Royal Astronomical Society*, **483**, 152
- Arca-Sedda M., Gualandris A., 2018, *MNRAS*, **477**, 4423
- Arca Sedda M., Mapelli M., Spera M., Benacquista M., Giacobbo N., 2020, *ApJ*, **894**, 133

- Askar A., Szkudlarek M., Gondek-Rosińska D., Giersz M., Bulik T., 2017, *MNRAS*, **464**, L36
- Askar A., Arca Sedda M., Giersz M., 2018, *MNRAS*, **478**, 1844
- Ballone A., Costa G., Mapelli M., MacLeod M., 2022, arXiv e-prints, p. [arXiv:2204.03493](https://arxiv.org/abs/2204.03493)
- Banerjee S., 2017, *MNRAS*, **467**, 524
- Banerjee S., 2018, *MNRAS*, **473**, 909
- Banerjee S., 2021a, arXiv e-prints, p. [arXiv:2109.14612](https://arxiv.org/abs/2109.14612)
- Banerjee S., 2021b, *MNRAS*, **500**, 3002
- Banerjee S., Baumgardt H., Kroupa P., 2010, *MNRAS*, **402**, 371
- Bavera S. S., et al., 2021, *A&A*, **647**, A153
- Belczynski K., Kalogera V., Bulik T., 2002, *ApJ*, **572**, 407
- Belczynski K., Kalogera V., Rasio F. A., Taam R. E., Zezas A., Bulik T., Maccarone T. J., Ivanova N., 2008, *ApJS*, **174**, 223
- Belczynski K., Bulik T., Fryer C. L., Ruiter A., Valsecchi F., Vink J. S., Hurley J. R., 2010, *ApJ*, **714**, 1217
- Belczynski K., Holz D. E., Bulik T., O’Shaughnessy R., 2016, *Nature*, **534**, 512
- Belczynski K., et al., 2020, *A&A*, **636**, A104
- Benacquista M. J., Downing J. M. B., 2013, *Living Reviews in Relativity*, **16**, 4
- Bethe H. A., Brown G. E., 1998, *ApJ*, **506**, 780
- Bouffanais Y., Mapelli M., Gerosa D., Di Carlo U. N., Giacobbo N., Berti E., Baibhav V., 2019, *ApJ*, **886**, 25
- Bouffanais Y., Mapelli M., Santoliquido F., Giacobbo N., Iorio G., Costa G., 2021a, *MNRAS*, **505**, 3873
- Bouffanais Y., Mapelli M., Santoliquido F., Giacobbo N., Di Carlo U. N., Rastello S., Artale M. C., Iorio G., 2021b, *MNRAS*, **507**, 5224
- Campanelli M., Lousto C. O., Zlochower Y., Merritt D., 2007, *Phys. Rev. Lett.*, **98**, 231102
- Carr B., Kühnel F., Sandstad M., 2016, *Phys. Rev. D*, **94**, 083504
- Cartwright A., Whitworth A. P., 2004, *MNRAS*, **348**, 589
- Chattopadhyay D., Hurley J., Stevenson S., Raidani A., 2022, *MNRAS*, **513**, 4527
- Claeys J. S. W., Pols O. R., Izzard R. G., Vink J., Verbunt F. W. M., 2014, *A&A*, **563**, A83
- Costa G., Bressan A., Mapelli M., Marigo P., Iorio G., Spera M., 2021, *MNRAS*, **501**, 4514
- Costa G., Ballone A., Mapelli M., Bressan A., 2022, *MNRAS*
- Crowther P. A., Schnurr O., Hirschi R., Yusof N., Parker R. J., Goodwin S. P., Kassim H. A., 2010, *MNRAS*, **408**, 731
- Dall’Amico M., Mapelli M., Di Carlo U. N., Bouffanais Y., Rastello S., Santoliquido F., Ballone A., Arca Sedda M., 2021, *MNRAS*, **508**, 3045
- Di Carlo U. N., Giacobbo N., Mapelli M., Pasquato M., Spera M., Wang L., Haardt F., 2019, *MNRAS*, **487**, 2947
- Di Carlo U. N., Mapelli M., Bouffanais Y., Giacobbo N., Santoliquido F., Bressan A., Spera M., Haardt F., 2020a, *MNRAS*, **497**, 1043
- Di Carlo U. N., et al., 2020b, *MNRAS*, **498**, 495
- Di Carlo U. N., et al., 2021, *MNRAS*, **507**, 5132
- Doctor Z., Wysocki D., O’Shaughnessy R., Holz D. E., Farr B., 2020, *ApJ*, **893**, 35
- Dominik M., Belczynski K., Fryer C., Holz D. E., Berti E., Bulik T., Mandel I., O’Shaughnessy R., 2012, *ApJ*, **759**, 52
- Dominik M., Belczynski K., Fryer C., Holz D. E., Berti E., Bulik T., Mandel I., O’Shaughnessy R., 2013, *ApJ*, **779**, 72
- Downing J. M. B., Benacquista M. J., Giersz M., Spurzem R., 2010, *MNRAS*, **407**, 1946
- Farr W. M., Stevenson S., Miller M. C., Mandel I., Farr B., Vecchio A., 2017, *Nature*, **548**, 426
- Favata M., Hughes S. A., Holz D. E., 2004, *ApJ*, **607**, L5
- Fishbach M., Holz D. E., Farr B., 2017, *ApJ*, **840**, L24
- Fragione G., Kocsis B., 2018, *Phys. Rev. Lett.*, **121**, 161103
- Fryer C. L., Belczynski K., Wiktorowicz G., Dominik M., Kalogera V., Holz D. E., 2012, *ApJ*, **749**, 91
- Fujii M. S., Tanikawa A., Makino J., 2017, *PASJ*, **69**, 94
- García F., Simaz Bunzel A., Chaty S., Porter E., Chassande-Mottin E., 2021, *A&A*, **649**, A114
- Georgiev I. Y., Böker T., Leigh N., Lützgendorf N., Neumayer N., 2016, *MNRAS*, **457**, 2122
- Gerosa D., Berti E., 2017, *Phys. Rev. D*, **95**, 124046
- Gerosa D., Berti E., O’Shaughnessy R., Belczynski K., Kesden M., Wysocki D., Gladysz W., 2018, *Phys. Rev. D*, **98**, 084036
- Giacobbo N., Mapelli M., 2018, *MNRAS*, **480**, 2011
- Giacobbo N., Mapelli M., 2019, *MNRAS*, **482**, 2234
- Giacobbo N., Mapelli M., 2020, *ApJ*, **891**, 141
- Giacobbo N., Mapelli M., Spera M., 2018, *MNRAS*, **474**, 2959
- Gieles M., Portegies Zwart S. F., Baumgardt H., Athanassoula E., Lamers H. J. G. L. M., Sipior M., Leenaarts J., 2006, *MNRAS*, **371**, 793
- Giersz M., Askar A., Wang L., Hypki A., Leveque A., Spurzem R., 2019, *MNRAS*, **487**, 2412
- Goswami S., Kiel P., Rasio F. A., 2014, *ApJ*, **781**, 81
- Heggie D. C., 1975, *MNRAS*, **173**, 729
- Heggie D., Hut P., 2003, *The Gravitational Million-Body Problem: A Multidisciplinary Approach to Star Cluster Dynamics*
- Hills J. G., Fullerton L. W., 1980, *AJ*, **85**, 1281
- Hoang B.-M., Naoz S., Kocsis B., Rasio F. A., Dosopoulou F., 2018, *ApJ*, **856**, 140
- Hurley J. R., Tout C. A., Pols O. R., 2002, *MNRAS*, **329**, 897
- Kimball C., Talbot C., Berry C. P. L., Carney M., Zevin M., Thrane E., Kalogera V., 2020, *ApJ*, **900**, 177
- Kroupa P., 2001, *MNRAS*, **322**, 231
- Kruckow M. U., Tauris T. M., Langer N., Kramer M., Izzard R. G., 2018, *MNRAS*, **481**, 1908
- Krumholz M. R., McKee C. F., Bland-Hawthorn J., 2019, *ARA&A*, **57**, 227
- Kuhn M. A., Hillenbrand L. A., Sills A., Feigelson E. D., Getman K. V., 2019, *ApJ*, **870**, 32
- Kumamoto J., Fujii M. S., Tanikawa A., 2019, *MNRAS*, **486**, 3942
- Kumamoto J., Fujii M. S., Tanikawa A., 2020, *MNRAS*, **495**, 4268
- Küpper A. H. W., Maschberger T., Kroupa P., Baumgardt H., 2011, *MNRAS*, **417**, 2300
- Lada C. J., Lada E. A., 2003, *ARA&A*, **41**, 57
- Loeb A., 2016, *ApJ*, **819**, L21
- Maggiore M., 2018, *Gravitational Waves: Volume 2: Astrophysics and Cosmology. Gravitational Waves*, Oxford University Press, <https://books.google.it/books?id=32NODwAAQBAJ>
- Makino J., Aarseth S. J., 1992, *PASJ*, **44**, 141
- Mandel I., de Mink S. E., 2016, *MNRAS*, **458**, 2634
- Mapelli M., 2016, *MNRAS*, **459**, 3432
- Mapelli M., Giacobbo N., 2018, *MNRAS*, **479**, 4391
- Mapelli M., Zampieri L., Ripamonti E., Bressan A., 2013, *MNRAS*, **429**, 2298
- Mapelli M., Giacobbo N., Ripamonti E., Spera M., 2017, *MNRAS*, **472**, 2422
- Mapelli M., Giacobbo N., Santoliquido F., Artale M. C., 2019, *MNRAS*
- Mapelli M., Spera M., Montanari E., Limongi M., Chieffi A., Giacobbo N., Bressan A., Bouffanais Y., 2020, *ApJ*, **888**, 76
- Mapelli M., et al., 2021, *MNRAS*, **505**, 339
- Mapelli M., Bouffanais Y., Santoliquido F., Arca Sedda M., Artale M. C., 2022, *MNRAS*, **511**, 5797
- Marchant P., Langer N., Podsiadlowski P., Tauris T. M., Moriya T. J., 2016, *A&A*, **588**, A50
- McKernan B., Ford K. E. S., Lyra W., Perets H. B., 2012, *MNRAS*, **425**, 460
- McKernan B., et al., 2018, *ApJ*, **866**, 66
- Mehta A. K., Buonanno A., Gair J., Miller M. C., Farag E., deBoer R. J., Wiescher M., Timmes F. X., 2022, *ApJ*, **924**, 39
- Mennekens N., Vanbeveren D., 2014, *A&A*, **564**, A134
- Miller M. C., Lauburg V. M., 2009, *ApJ*, **692**, 917
- Moe M., Di Stefano R., 2017, *ApJS*, **230**, 15
- Neijssel C. J., et al., 2019, *MNRAS*, **490**, 3740

- Ng K. K. Y., Vitale S., Farr W. M., Rodriguez C. L., 2021, *ApJ*, **913**, L5
- Nitadori K., Aarseth S. J., 2012, *MNRAS*, **424**, 545
- Nitz A. H., et al., 2020, *ApJ*, **891**, 123
- Nitz A. H., Capano C. D., Kumar S., Wang Y.-F., Kastha S., Schäfer M., Dhurkunde R., Cabero M., 2021, *ApJ*, **922**, 76
- O’Leary R. M., Kocsis B., Loeb A., 2009, *MNRAS*, **395**, 2127
- Olsen S., Venumadhav T., Mushkin J., Roulet J., Zackay B., Zaldarriaga M., 2022, *Phys. Rev. D*, **106**, 043009
- Perna R., Wang Y.-H., Farr W. M., Leigh N., Cantiello M., 2019, *ApJ*, **878**, L1
- Peters P. C., 1964, *Physical Review*, **136**, 1224
- Portegies Zwart S. F., McMillan S. L. W., 2002, *ApJ*, **576**, 899
- Portegies Zwart S. F., Yungelson L. R., 1998, *A&A*, **332**, 173
- Portegies Zwart S. F., McMillan S. L. W., Gieles M., 2010, *ARA&A*, **48**, 431
- Rastello S., Amaro-Seoane P., Arca-Sedda M., Capuzzo-Dolcetta R., Fragione G., Tosta e Melo I., 2019, *MNRAS*, **483**, 1233
- Rastello S., Mapelli M., Di Carlo U. N., Giacobbo N., Santoliquido F., Spera M., Ballone A., Iorio G., 2020, *MNRAS*, **497**, 1563
- Rastello S., Mapelli M., Di Carlo U. N., Iorio G., Ballone A., Giacobbo N., Santoliquido F., Torriamenti S., 2021, *MNRAS*, **507**, 3612
- Renzo M., Cantiello M., Metzger B. D., Jiang Y. F., 2020, *ApJ*, **904**, L13
- Rizzuto F. P., et al., 2021, *MNRAS*, **501**, 5257
- Rodriguez C. L., Morscher M., Pattabiraman B., Chatterjee S., Haster C.-J., Rasio F. A., 2015, *Physical Review Letters*, **115**, 051101
- Rodriguez C. L., Chatterjee S., Rasio F. A., 2016a, *Phys. Rev. D*, **93**, 084029
- Rodriguez C. L., Zevin M., Pankow C., Kalogera V., Rasio F. A., 2016b, *ApJ*, **832**, L2
- Rodriguez C. L., Amaro-Seoane P., Chatterjee S., Kremer K., Rasio F. A., Samsing J., Ye C. S., Zevin M., 2018, *Phys. Rev. D*, **98**, 123005
- Rodriguez C. L., Zevin M., Amaro-Seoane P., Chatterjee S., Kremer K., Rasio F. A., Ye C. S., 2019, *Phys. Rev. D*, **100**, 043027
- Roulet J., Chia H. S., Olsen S., Dai L., Venumadhav T., Zackay B., Zaldarriaga M., 2021, *Phys. Rev. D*, **104**, 083010
- Samsing J., 2018, *Phys. Rev. D*, **97**, 103014
- Samsing J., D’Orazio D. J., 2018, *MNRAS*, **481**, 5445
- Samsing J., Askar A., Giersz M., 2018, *ApJ*, **855**, 124
- Sana H., Evans C. J., 2011, in Neiner C., Wade G., Meynet G., Peters G., eds, IAU Symposium Vol. 272, Active OB Stars: Structure, Evolution, Mass Loss, and Critical Limits. pp 474–485 ([arXiv:1009.4197](https://arxiv.org/abs/1009.4197)), doi:10.1017/S1743921311011124
- Sana H., et al., 2012, *Science*, **337**, 444
- Sánchez N., Alfaro E. J., 2009, *ApJ*, **696**, 2086
- Spera M., Mapelli M., Giacobbo N., Trani A. A., Bressan A., Costa G., 2019, *MNRAS*, **485**, 889
- Spitzer L., 1987, *Dynamical evolution of globular clusters*. Princeton University Press
- Stevenson S., Berry C. P. L., Mandel I., 2017, *MNRAS*, **471**, 2801
- Stone N. C., Metzger B. D., Haiman Z., 2017, *MNRAS*, **464**, 946
- Tang P. N., Eldridge J. J., Stanway E. R., Bray J. C., 2020, *MNRAS*, **493**, L6
- Torriamenti S., Ballone A., Mapelli M., Gaspari N., Di Carlo U. N., Rastello S., Giacobbo N., Pasquato M., 2021, *MNRAS*, **507**, 2253
- Tutukov A., Yungelson L., 1973, *Nauchnye Informatsii*, **27**, 70
- VanLandingham J. H., Miller M. C., Hamilton D. P., Richardson D. C., 2016, *ApJ*, **828**, 77
- Venumadhav T., Zackay B., Roulet J., Dai L., Zaldarriaga M., 2019, *Phys. Rev. D*, **100**, 023011
- Venumadhav T., Zackay B., Roulet J., Dai L., Zaldarriaga M., 2020, *Phys. Rev. D*, **101**, 083030
- Vitale S., Lynch R., Raymond V., Sturani R., Veitch J., Graff P., 2017, *Phys. Rev. D*, **95**, 064053
- Wang L., Spurzem R., Aarseth S., Nitadori K., Berczik P., Kouwenhoven M. B. N., Naab T., 2015, *MNRAS*, **450**, 4070
- Wang L., et al., 2016, *MNRAS*, **458**, 1450
- Webbink R. F., 1984, *ApJ*, **277**, 355
- Wong K. W. K., Gerosa D., 2019, *Phys. Rev. D*, **100**, 083015
- Wong K. W. K., Breivik K., Kremer K., Callister T., 2021, *Phys. Rev. D*, **103**, 083021
- Yang Y., Bartos I., Haiman Z., Kocsis B., Márka Z., Stone N. C., Márka S., 2019, *ApJ*, **876**, 122
- Zevin M., Pankow C., Rodriguez C. L., Sampson L., Chase E., Kalogera V., Rasio F. A., 2017, *ApJ*, **846**, 82
- Zevin M., Samsing J., Rodriguez C., Haster C.-J., Ramirez-Ruiz E., 2019, *ApJ*, **871**, 91
- Zevin M., et al., 2021, *ApJ*, **910**, 152
- Ziosi B. M., Mapelli M., Branchesi M., Tormen G., 2014, *MNRAS*, **441**, 3703
- de Mink S. E., Belczynski K., 2015, *ApJ*, **814**, 58
- de Mink S. E., Mandel I., 2016, *MNRAS*, **460**, 3545
- du Buisson L., et al., 2020, *MNRAS*, **499**, 5941

This paper has been typeset from a  $\text{\TeX}/\text{\LaTeX}$  file prepared by the author.